UC Berkeley
UC Berkeley Previously Published Works

Title
Computational investigation of chalcogenide spinel conductors for all-solid-state Mg batteries

Permalink

Journal
Chemical Communications, 56(13)

ISSN
1359-7345

Authors
Koettgen, Julius
Bartel, Christopher J
Ceder, Gerbrand

Publication Date
2020-02-13

DOI
10.1039/c9cc09510a

Peer reviewed

a. Materials Sciences Division, Lawrence Berkeley National Laboratory, Berkeley, CA 94720, USA.

b. Department of Materials Science and Engineering, University of California, Berkeley, Berkeley, CA 94720, USA

COMMUNICATION

## Computational investigation of chalcogenide spinel conductors for all-solid-state Mg batteries

Julius Koettgen[a], Christopher J. Bartel[b], and Gerbrand Ceder[a,b,†]

Seven MgLn$_2$X$_4$ (Ln = lanthanoid, X = S, Se) spinels are calculated with density functional theory to have low barriers for Mg migration (< 380 meV) and are stable or nearly stable (within 50 meV/atom of stability with respect to competing structures and compositions). As the size of the Ln increases, Mg mobility is found to increase, but stability in the spinel structure is found to decrease.

Magnesium batteries are an interesting alternative to Li-ion technology because of the potential for improved safety and higher energy density.[1–3] The ability to use Mg metal as an anode is beneficial because of its high volumetric energy density (3830 mAh/mL) relative to that of graphite (700 mAh/mL), which is generally employed as an anode in Li-ion batteries using liquid or polymer gel electrolytes.[4] Only a few good liquid electrolytes exist for Mg batteries as Mg metal cannot be deposited reversibly in electrolytes that react with the metal. For this reason, we recently explored whether solid electrolytes with sufficient Mg-ion conductivity exist.[5] Unlike for Li and Na, for which a large number of solids with very high ionic conductivity have been reported,[6,7] virtually no solids with high Mg-ion conductivity have been identified, apart from a few so-far unconfirmed computational predictions.[8]

Materials with high Li conductivity have been shown to possess low Mg mobility because the higher charge density of divalent Mg relative to that of monovalent Li leads to stronger electrostatic interactions with the host lattice.[9] Recently, two design principles to improve mobility in multivalent solids have been proposed. First, structures where the multivalent ion sits in a site where it has an unfavourable coordination environment have been observed to have lower migration barriers, in particular when the activated state is closer to the preferred coordination.[7,9–11] Superior Mg^{2+} mobility was previously observed in spinels (**Fig. 1a**) with composition TM$_2$X$_4$ (TM = Ti, Cr, Mn, Fe, Co, Ni and X = O, S), where the diffusing ion resides in a tetrahedral site but migrates through an activated octahedral coordination as shown in **Fig 1b**.[9,10,12–14] Second, Mg^{2+} mobility is generally higher for sulphides than oxides,

suggesting that the inclusion of larger, more polarizable anions helps decrease the electrostatic interaction between the working ion and the host structure.[10,14]
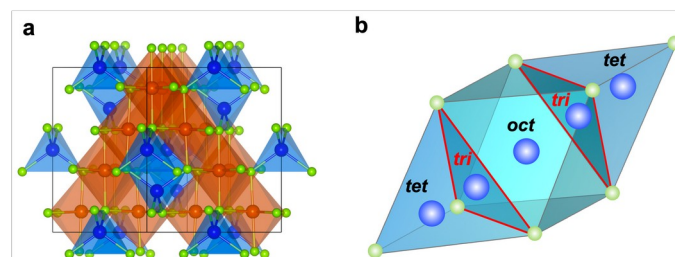

Figure 1. **a)** MgLn$_2$X$_4$ spinel structure where Mg is blue, the lanthanoid (Ln) is orange, and the chalcogenide (X) is light green, **b)** Diffusion path for Mg^{2+} (blue) from the tetrahedral site, *tet*, through the face-sharing triangular state, *tri*, then the octahedral site, *oct*. The diffusion path is locally symmetric such that before returning to *tet*, Mg^{2+} again passes through *tri*.

These design principles led to the investigation of magnesium spinel chalcogenides MgM$_2$X$_4$ with M = Sc, In, Y and X = S, Se, Te.[5] Several of these compositions have been reported experimentally, including MgSc$_2$S$_4$,[15] MgIn$_2$S$_4$,[15,16] MgSc$_2$Se$_4$,[17] and MgY$_2$Se$_4$.[17] The calculated barriers for Mg^{2+} migration generally decrease from sulphides to selenides to tellurides as both the unit cell volume and the polarizability of the anion increase. In MgSc$_2$Se$_4$, *ab initio* calculations and nuclear magnetic resonance experiments indicate a Mg^{2+} migration barrier of 380 meV, comparable to barriers in Li-ion cathode materials.[18] In this work, we demonstrate that Mg^{2+} mobility can be further increased through the incorporation of large cations from the lanthanide series. However, destabilization of the spinel structure occurs upon increasing the size of the lanthanoid; therefore, the optimal spinel Mg conductor balances high mobility and synthesizability.

The Mg^{2+} mobility and stability of magnesium chalcogenide spinels, MgLn$_2$X$_4$, with Ln = Lu, Tm, Er, Ho, Dy, Tb, Sm, Pm, Nd, Pr, La and X = S, Se were investigated using density functional theory

(DFT) in the generalized gradient approximation (GGA)[19] and the nudged elastic band method (NEB)[20] for Mg^{2+} mobility calculations. Meta-GGA[21] was used for stability calculations. Substituting larger lanthanoids into the spinel increases the unit cell volume, as shown in **Fig. 2a**. A 40% increase of the cation radius, r_{Ln}, from 0.745 Å (Sc^{3+})[22] to 1.032 Å (La^{3+})[22], leads to a unit cell volume increase of ~30%. **Fig. 2b** shows the calculated Mg^{2+} migration barrier in these spinels assuming vacancy-mediated diffusion. The increase in volume to accommodate larger cations does indeed correlate with an improved Mg^{2+} mobility, as the calculated migration barriers decrease from 375 meV for $MgSc_2Se_4$[5] to 290 meV for $MgLa_2Se_4$. In fact, the barriers calculated for all materials are lower than that of the previously synthesized $MgSc_2Se_4$. The Mg^{2+} migration barrier decreases nearly linearly with r_{Ln}, with the notable exception of $MgLa_2S_4$, which is associated with the destabilization of Mg in the octahedral state as discussed later.
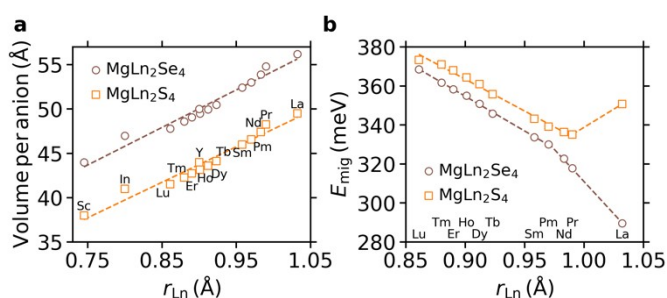
Figure 2. **a)** Effect of Ln ionic radius, r_{Ln}, on the calculated unit cell volume of the spinel structure, **b)** Effect of r_{Ln} on the vacancy-mediated Mg^{2+} migration barrier, E_{mig}. Ionic radii are from Shannon[22]. Results for Sc, In, and Y are from ref. [5]. In both panels, the dashed lines are drawn to guide the eye.

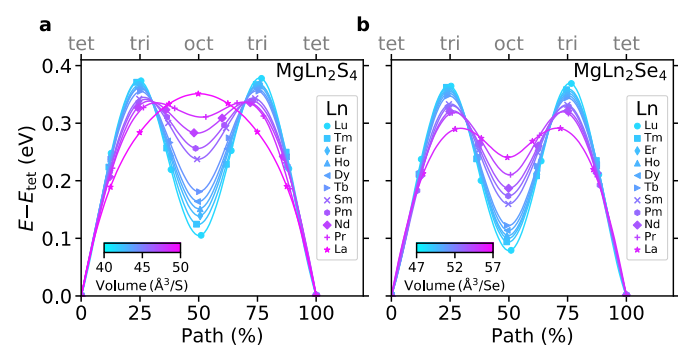The energy profiles along the Mg^{2+} migration path are shown in **Fig. 3**. All compounds show a global minimum with Mg in a tetrahedral site (*tet*), confirming that it is a locally stable site in these spinel structures. All compounds except $MgLa_2S_4$ show a local minimum for the octahedral state (*oct*), and the transition state (highest energy along the path) occurs when Mg^{2+} passes through the triangular face (*tri*) that is shared between *tet* and *oct*. Of particular importance for Mg^{2+} migration is the distance between the migrating Mg^{2+} and neighbouring chalcogenides (X), as the electron density of these anions impedes cation transport. Assuming regular polyhedra, the minimum distance between the centroid (Mg^{2+}) and vertex (X^{2-}) of each environment is proportional

to $\quad \dfrac{d_{XX}}{\sqrt{3}} \approx 0.57\, d_{XX}, \qquad \dfrac{3\, d_{XX}}{2\sqrt{6}} \approx 0.61\, d_{XX}, \qquad$ and

$\dfrac{d_{XX}}{\sqrt{2}} \approx 0.71\, d_{XX}$ for *tri*, *tet*, and *oct*, respectively, where d_{XX} is the X–X bond distance that forms the shared edge of the octahedron and tetrahedron. This relationship dictates that *tri* will have the smallest Mg-X distance and therefore likely be the highest energy (transition) state as long as *oct* and *tet* are local minima in the energy profile. For $MgLa_2S_4$, *oct* is not a local minimum and the

migration barrier for this material is therefore determined by $E_{oct} - E_{tet}$.

Figure 3. Energy profiles for vacancy-mediated Mg^{2+} migration in sulphides (**a**) and selenides (**b**). Energy is shown relative to the tetrahedral Mg state ($E - E_{tet}$). The colourbar provides the volume per anion of the pristine structure.

The Mg^{2+} migration energy, E_{mig}, is compared to the energy of the octahedral state relative to the tetrahedral state ($E_{oct} - E_{tet}$) in **Fig 4**. The energies of the *tri* and *oct* states (relative to *tet*) change in opposite directions as the structure expands to accommodate larger and larger Ln's. *tri* is stabilized with increasing r_{Ln} because this state requires unfavourably small Mg-X distances as Mg^{2+} passes through the triangular face, and structure expansion lengthens this distance. The destabilization of *oct* when r_{Ln} is increased can be attributed to the relatively small size of Mg^{2+}. This is reflected in the ground-state structures for MgX compounds – MgS is rock salt with octahedral Mg coordination but increasing r_X to MgSe changes the preferred coordination to tetrahedral in wurtzite (ground-state structures determined with GGA). The preference for coordination of a cation, *c*, by an anion, *a*, can be estimated by classic radii ratio rules[23] where tetrahedral coordination is expected for $0.225 < r_c/r_a \le 0.414$ and octahedral coordination for $0.414 < r_c/r_a \le 0.732$. For Mg^{2+}, the radius ratio is 0.391 for sulphides and 0.364 for selenides, suggesting Mg^{2+} should prefer large tetrahedral or small octahedral environments for these chalcogenides. The octahedral Mg-X bond distance in MgS is ~2.61 Å and expands from ~2.73 (2.85) Å in $MgLu_2S_4$ ($MgLu_2Se_4$) to ~2.85 (2.96) Å in $MgLa_2S_4$ ($MgLa_2Se_4$) as r_{Ln} increases in these spinels. The unfavourably expanded MgX_6 octahedra in the $MgLn_2X_4$ spinels accounts for the destabilization of *oct* relative to *tet* as r_{Ln} increases.
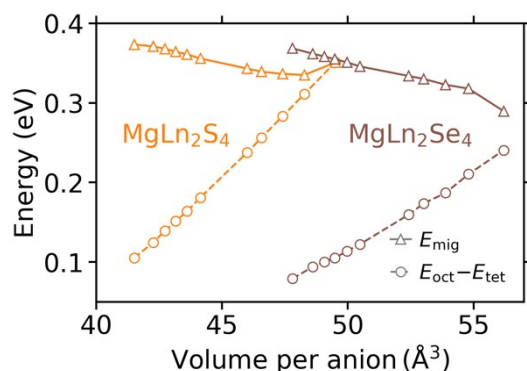
Figure 4. Comparing the Mg^{2+} migration energy, E_{mig}, to the difference in octahedral and tetrahedral energies, $E_{oct}-E_{tet}$ as a function of the calculated volume per anion in the pristine structures.

One of the motivations for studying spinel conductors is that they flatten the migration energy profile by stabilizing tetrahedral Mg and enabling Mg to pass through a more stable octahedral configuration during migration. This principle suggests that minimizing the difference in energy between the *oct* and *tet* states would lead to the lowest possible migration barriers because the energy profile is maximally flat when $E_{oct} = E_{tet}$. However, within this group of $MgLn_2X_4$ compounds, we find instead that maximizing this energy difference results in the lowest migration barriers (with the exception of $MgLa_2S_4$) because the area of the face-sharing triangle is largest (most stable) when the MgX_6 octahedra is largest (least stable).

Finally, the stability of the spinel structure relative to competing polymorphs and competing compounds was investigated using the revised-TPSS meta-GGA density functional.[21] Meta-GGA's have been shown to be superior to GGA in determining the ground-state structure[24] and stability[25] of chalcogenides. In **Fig. 5**, the energy above the convex hull of stable compounds in each chemical space, E_{hull},[14,26] is shown for all compounds in five different structures typically observed for AB_2X_4 compounds.[27] Experimentally known structures for each compound are highlighted along the top of **Fig. 5**. Stable compounds have $E_{hull} = 0$, and synthesized sulphides and selenides have been observed to be metastable up to $E_{hull} \approx 50$ meV/atom.[28] An even wider range of accessible metastability is expected for spinels because of their especially low surface energy, which may result in preferential nucleation during synthesis.[29]

$MgLu_2S_4$, $MgLu_2Se_4$, $MgTm_2Se_4$, and $MgEr_2Se_4$ were calculated to have $E_{hull} < 25$ meV/atom and spinel as the lowest energy structure at that composition. Additionally, $MgTm_2S_4$, $MgEr_2S_4$, and $MgHo_2Se_4$ have $E_{hull} < 50$ meV/atom in the spinel structure but MnY_2S_4 is the lowest energy polymorph. On this basis, these seven materials are considered potentially synthesizable in the spinel structure. Indeed, all but $MgEr_2S_4$ have been reported to crystallize in the spinel structure ($MgTm_2S_4$ has been reported in both spinel and MnY_2S_4 structures).[27,30] Our calculations are generally consistent with the experimental observations as the experimentally observed crystal structure is calculated to be the lowest energy structure at $MgLn_2X_4$ for 9 of 10 materials (all except $MgHo_2Se_4$), and all 10 experimentally observed structures are calculated to be stable or nearly stable ($E_{hull} < 50$ meV/atom).[27,30]
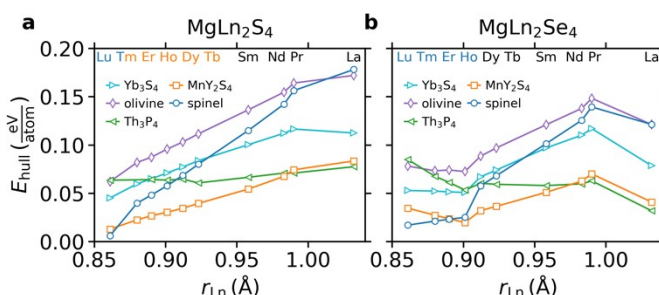
Figure 5. Stability with respect to competing phases, E_{hull}, for each sulphide **(a)** and selenide **(b)** in a variety of crystal structures common to AB_2X_4-type compounds. The colour of each element at the top of both panels correspond with the experimentally observed crystal structure for that composition.[27,30] $MgTm_2S_4$ is coloured for both spinel and MnY_2S_4 because both crystal structures have been reported. Elements coloured black indicate no experimentally known crystal structure.

The calculated sequence of stable crystal structures can be understood by considering the Ln coordination environment. At low r_{Ln}, spinel is the lowest energy structure, then MnY_2S_4 becomes the lowest energy for intermediate r_{Ln}, and the Th_3P_4 structure is the most stable polymorph for the largest Ln's. The Ln coordination number increases from 6 in spinel to 6/7 in MnY_2S_4 to 8 in Th_3P_4, stabilizing the larger and larger Ln. The larger selenium stabilizes spinel for larger Ln, up to at least Ho, whereas spinel is the calculated ground-state only for Ln=Lu among the sulphides.

Increasing the size of the cation in chalcogenide spinels decreases the Mg^{2+} migration barrier. However, increasing the cation size also leads to a preference for non-spinel structures and a general destabilization relative to competing compounds. The spinel structure has the advantage of placing Mg in its less stable tetrahedral configuration, decreasing the Mg migration barrier; however, this advantage is balanced by energetically preferred alternative structures for large cations. Still, we predict $MgLu_2S_4$, $MgLu_2Se_4$, $MgTm_2S_4$, $MgTm_2Se_4$, $MgEr_2S_4$, $MgEr_2Se_4$, and $MgHo_2Se_4$ to be candidate solid-state electrolytes that strike a balance between relatively small Mg migration energies ($E_{mig} < 380$ meV) and relatively good stability ($E_{hull} < 50$ meV/atom) in the spinel structure.

Methods

The stability and Mg mobility of the investigated materials were calculated with density functional theory (DFT)[31] using the Vienna Ab Initio Simulation Package (VASP)[32]. For mobility calculations, the generalized gradient approximation (GGA) according to Perdew, Burke, and Ernzerhof (PBE)[33] and the projector augmented-wave (PAW) method[34] were used with an energy cut-off of 520 eV for plane waves. $2 \times 2 \times 2$ supercells, e.g., $Mg_{16}La_{32}Se_{64}$ and $(Mg_{15}La_{32}Se_{64})^{2-}$, were calculated using a $2 \times 2 \times 2$ Monkhorst–Pack k-point mesh. The positions of the atoms and the cell volume were optimized for the pristine structure. For the subsequent mobility calculations with one Mg^{2+} vacancy, only the positions of the ions were optimized. Electronic and ionic relaxations were performed with convergence parameters of 10^{-5} eV and 10^{-2} eV $Å^{-1}$, respectively. The Mg^{2+} vacancy was charge-balanced by a neutralizing background charge. The minimum energy pathways were calculated by linearly interpolating seven images between the optimized initial and final structures and subsequently applying the nudged elastic band (NEB) method.[35] For the stability calculations, the revised-TPSS self-consistent meta-GGA[36] within the PAW method was used to calculate all $MgLn_2X_4$ compounds in each of the five prototype structures – spinel, MnY_2S_4, Th_3P_4, olivine, and Yb_3S_4 – and all relevant competing phases available in the Materials Project.[37] All calculated results are available as a table in the **Supplementary Information**.

Conflicts of interest

˙There are no conflicts to declare.

Notes and references

1 P. Canepa, G. Sai Gautam, D. C. Hannah, R. Malik, M. Liu, K. G. Gallagher, K. A. Persson and G. Ceder, *Chem. Rev.*, 2017, **117**, 4287–4341.

2 J. Muldoon, C. B. Bucur and T. Gregory, *Chem. Rev.*, 2014, **114**, 11683–11720.

3 J. Bitenc and R. Dominko, *Frontiers in Chemistry*, 2018, **6**, 634.

4 H. D. Yoo, I. Shterenberg, Y. Gofer, G. Gershinsky, N. Pour and D. Aurbach, *Energy Environ. Sci.*, 2013, **6**, 2265–2279.

5 P. Canepa, S.-H. Bo, G. Sai Gautam, B. Key, W. D. Richards, T. Shi, Y. Tian, Y. Wang, J. Li and G. Ceder, *Nat. Commun.*, 2017, **8**, 1759.

6 T. Famprikis, P. Canepa, J. A. Dawson, M. S. Islam and C. Masquelier, *Nature Materials*, 2019, **18**, 1278–1291.

7 Y. Wang, W. D. Richards, S. P. Ong, L. J. Miara, J. C. Kim, Y. Mo, G. Ceder, *Nat. Mater.*, 2015, **14**, 1026–1031.

8 Z. Rong, P. Xiao, M. Liu, W. Huang, D. C. Hannah, W. Scullin, K. A. Persson and G. Ceder, *Chem. Commun.*, 2017, **53**, 7998–8001.

9 Z. Rong, R. Malik, P. Canepa, G. Sai Gautam, M. Liu, A. Jain, K. Persson and G. Ceder, *Chem. Mater.*, 2015, **27**, 6016–6021.

10 M. Liu, Z. Rong, R. Malik, P. Canepa, A. Jain, G. Ceder and K. A. Persson, *Energy Environ. Sci.*, 2015, **8**, 964–974.

11 G. Sai Gautam, P. Canepa, A. Abdellahi, A. Urban, R. Malik and G. Ceder, *Chem. Mater.*, 2015, **27**, 3733–3742.

12 I. D. Brown, *Acta Crystallogr. B*, 1988, **44**, 545–553.

13 V. V. Kulish, D. Koch and S. Manzhos, *Phys. Chem. Chem. Phys.*, 2017, **19**, 6076–6081.

14 M. Liu, A. Jain, Z. Rong, X. Qu, P. Canepa, R. Malik, G. Ceder and K. A. Persson, *Energy Environ. Sci.*, 2016, **9**, 3201–3209.

15 M. Patrie, J. Flahaut and L. Domage, *C. R. Hebd. Acad. Sci.*, 1964, **258**, 2585–2586.

16 W. M. Yim, A. K. Fan and E. J. Stofko, *J. Electrochem. Soc.*, 1973, **120**, 441.

17 M. Guittard, C. Souleau and H. Farsam, *Comptes Rendus Hebdomadaires des Seances de l'Academie des Sciences*, 1964, **259**, 2847–2849.

18 J. C. Bachman, S. Muy, A. Grimaud, H.-H. Chang, N. Pour, S. F. Lux, O. Paschos, F. Maglia, S. Lupart, P. Lamp, L. Giordano and Y. Shao-Horn, *Chem. Rev.*, 2016, **116**, 140–162.

19 J. P. Perdew, K. Burke and M. Ernzerhof, *Phys. Rev. Lett.*, 1996, **77**, 3865–3868.

20 D. Sheppard, R. Terrell and G. Henkelman, *J. Chem. Phys.*, 2008, **128**, 134106.

21 J. Sun, M. Marsman, G. I. Csonka, A. Ruzsinszky, P. Hao, Y.-S. Kim, G. Kresse and J. P. Perdew, *Phys. Rev. B*, 2011, **84**, 035117.

22 R. D. Shannon, *Acta Crystallogr. A*, 1976, **32**, 751–767.

23 V. M. Goldschmidt, *Trans. Faraday Soc.*, 1929, **25**, 253–283.

24 J. H. Yang, D. A. Kitchaev and G. Ceder, *Phys. Rev. B*, 2019, **100**, 035132.

25 C. J. Bartel, A. W. Weimer, S. Lany, C. B. Musgrave and A. M. Holder, *npj Computational Materials*, 2019, **5**, 4.

26 S. P. Ong, L. Wang, B. Kang and G. Ceder, *Chem. Mater.*, 2008, **20**, 1798–1807.

27 O. Müller and R. Roy, *The major ternary structural families*, Springer-Verlag, 1974.

28 W. Sun, S. T. Dacek, S. P. Ong, G. Hautier, A. Jain, W. D. Richards, A. C. Gamst, K. A. Persson and G. Ceder, *Science Advances*, 2016, **2**, e1600225.

29 A. Navrotsky, C. Ma, K. Lilova and N. Birkner, *Science*, 2010, **330**, 199.

30 J. Flahaut, in *Progress in Science and Technology of the Rare Earths*, Pergamon Press, 1968, pp. 209–283.

31 W. Kohn and L. J. Sham, *Phys. Rev.*, 1965, **140**, A1133–A1138.

32 G. Kresse and J. Furthmüller, *Physical Review B*, 1996, **54**, 11169.

33 J. P. Perdew, K. Burke and M. Ernzerhof, *Phys. Rev. Lett.*, 1996, **77**, 3865–3868.

34 G. Kresse and D. Joubert, *Phys. Rev. B*, 1999, **59**, 1758–1775.

35 D. Sheppard, R. Terrell and G. Henkelman, *The Journal of chemical physics*, 2008, **128**, 134106.

36 J. Sun, M. Marsman, G. I. Csonka, A. Ruzsinszky, P. Hao, Y.-S. Kim, G. Kresse and J. P. Perdew, *Phys. Rev. B*, 2011, **84**, 035117.

37 A. Jain, S. P. Ong, G. Hautier, W. Chen, W. D. Richards, S. Dacek, S. Cholia, D. Gunter, D. Skinner, G. Ceder and K. A. Persson, *APL Materials*, 2013, **1**, 011002.